

Xiaohui Su¹

School of Hydraulic Engineering,
Dalian University of Technology,
Dalian, Liaoning Province 116023, China
e-mail: sxh@dlut.edu.cn

Huiying Zhang

School of Energy and Power Engineering,
Dalian University of Technology,
Dalian, Liaoning Province 116023, China
e-mail: huiying.zhang@queensu.ca

Guang Zhao

School of Energy and Power Engineering,
Dalian University of Technology,
Dalian, Liaoning Province 116023, China
e-mail: zhaoguang@dlut.edu.cn

Yao Cao

School of Energy and Power Engineering,
Dalian University of Technology,
Dalian, Liaoning Province 116023, China
e-mail: 947268922@mail.dlut.edu.cn

Yong Zhao¹

School of Engineering,
Nazarbayev University,
Astana 010000, Republic of Kazakhstan
e-mail: yong.zhao@nu.edu.kz

Numerical and Experimental Investigations on the Hydrodynamic Performance of a Tidal Current Turbine

In this paper, numerical and experimental investigations are presented on the hydrodynamic performance of a horizontal tidal current turbine (TCT) designed and made by our Dalian University of Technology (DUT) research group. Thus, it is given the acronym: DUTTCT. An open-source computational fluid dynamics (CFD) solver, called PIMPLEDFM-FOAM, is employed to perform numerical simulations for design analysis, while experimental tests are conducted in a DUT towing tank. The important factors, including self-starting velocity, tip speed ratio (TSR), and yaw angle, which play important roles in the turbine output power, are studied in the investigations. Results obtained show that the maximum power efficiency of the newly developed turbine (DUTTCT) could reach up to 47.6%, and all its power efficiency is over 40% in the TSR range from 3.5 to 6; the self-starting velocity of DUTTCT is about 0.745 m/s; and the yaw angle has negligible influence on its efficiency as it is less than 10 deg. [DOI: 10.1115/1.4038249]

Introduction

Tidal current energy has been receiving more and more attention since the late 1990s, mainly due to four reasons: the increasing demand for electricity from all human activities; the depletion of fossil energy; the increasingly stringent regulations on CO₂ emission due to climate change considerations; and the last, also the most important one, the significant improvement of energy conversion technology [1–7]. The technology of energy conversion in the specialized field of tidal current energy is different from that of the tidal barrage, which is used to exploit the resources of the tidal range. The tidal current energy is harnessed by an underwater turbine located in a tidal current. Compared with the tidal barrage technology, the newly developed turbine technology has at least two advantages: (1) there is no need to build a barrage which requires a large amount of capital investment and (2) there is little negative impact on the environment and ecology in the neighborhood of the turbine.

The design theories and methods used for hydrofoil and blade design and turbine design, as well as equipment design, are important to achieve desirable turbine characteristics. For blade design for tidal current turbine (TCT), a commonly accepted method called the blade element momentum (BEM) theory can be employed [4]. For the implementation of the BEM theory, a blade is divided into multiple elements. For each element, its chord length and twist angle are determined as functions of its radius r based on the conservation laws of mass, momentum, and energy, which is based on the assumption that water flow around the element is two-dimensional and inviscid. However, the flow around a TCT is actually much more complicated than the previously mentioned assumption, and the flow can be

three-dimensional (3D) and turbulent. By using the computational fluid dynamics (CFD) technique, the hydrodynamic performances of TCTs can be fully and more accurately analyzed, especially for off-design conditions. Traditionally, only flow over one blade is simulated on a rotating coordinate system, with the assumption of periodic boundary conditions and steady flow due to the requirement of excessive computing power. Again, the actual flow is not exactly steady and the boundary condition not periodic. Recently with the availability of high-performance computing at low costs, it has now become possible for researchers to simulate flow over all the blades in a rotor, using two-equation turbulence models, Reynolds stress models, and even large eddy simulation [8]. It is even possible not only just to simulate the flow over the rotor but also the wake behind the rotor because the rotating flow in the wake is closely related to the static pressure there, although they may not greatly affect the power output of the turbine. To simulate this so-called whole flow field effects, it is necessary that the multiblock grid technology is employed to mesh the flow field with multiple blocks of meshes, including one block of mesh that wraps around the rotor, another block before the rotor, and a third one for the wake. The so-called multiple reference frame (MRF) method is commonly used in CFD studies to solve the flow field around TCT. The MRF method uses source terms to describe the influence of rotation, such as Coriolis and centrifugal forces, without actually rotating the mesh of the rotor. For instance, this approach is adopted in the commercial software ANSYS CFX solver and also in open-source solvers, such as MRFSIMPLEFOAM. The MRF method has been used in most of the numerical simulations for flows passing through tidal current/stream turbines [9–11].

The arbitrary Lagrangian Euler (ALE) method is an alternative way to calculate fluid flows around rotating machinery such as TCTs. Different from the MRF method using fixed Euler grids, the ALE method solves the Navier–Stokes governing equations with dynamic deformable and moving meshes. When the mesh is excessively deformed due to the movement of boundaries, mesh regeneration is normally performed to maintain mesh quality or a

¹Corresponding authors.

Contributed by the Ocean, Offshore, and Arctic Engineering Division of ASME for publication in the JOURNAL OF OFFSHORE MECHANICS AND ARCTIC ENGINEERING. Manuscript received March 6, 2016; final manuscript received October 13, 2017; published online November 16, 2017. Assoc. Editor: Yin Lu Young.

sliding mesh interface is used between two blocks of meshes with different speeds. The ALE method has the advantage of the Lagrangian method, which means that it could describe the boundary movement including rotation, translation, their combination, and even deformation of internal boundaries. The MRF method would be more accurate under the condition of higher degree of density (DOD), which is defined as the ratio of the cross-sectional area of blades to the sweeping area of the rotor, because there is no relative motion between the rotor and the stationary parts, and the rotating effects are simulated by using source terms, such as the Coriolis and centrifugal forces. The DOD becomes higher as the number of blades is increased, such as in the conventional stream turbine. However, the DOD for the tidal current/stream turbine is normally low, at about 20–30%, as the number of blades is only three. In order to overcome the disadvantage of the MRF, the ALE method can be used. There are two sets of grids in the computational domain: one for the stationary domain and the other for the rotating one. Between the rotating and stationary meshes, an arbitrary mesh interface (AMI) is used to connect the two different meshes through the interface so that the rotating one can rotate and slide against the stationary one while they remain in contact and communicate with each other.

PIMPLEDYMFOAM is an ALE solver using the hybrid pressure-implicit with splitting operators-semi-implicit method for pressure linked equation (PIMPLE) numerical solution algorithm and dynamic meshes (DYM) from the open-source software openFOAM4.x [12], and its predecessor, called TURBODYMFOAM. So far, there is only one paper [13] found in the literature on the numerical simulation of TCT by using TURBODYMFOAM, and no report on the use of PIMPLEDYMFOAM has been published.

Since both empirical models and CFD simulations are all based on certain assumptions, experimental testing is a crucial way to investigate the hydrodynamic performances of TCTs and validate the empirical and numerical models mentioned previously. Hydrodynamic tunnels or flume tanks have been used in experiments [14–17], which enable water to be pumped and flow through a turbine either in close circuit or in open circuit. Sensors are used to measure torque and thrust as well as the rotating speed of the turbine. Velocities of the current are measured by using flow probes, such as pitot tubes and laser Doppler anemometers. Beside flume tanks, towing tank facilities were also used in experiments [14–17]. A turbine is towed in the towing tank, and its rotor rotates due to relative incoming water flow. The hydrodynamic performance of a turbine can be determined through the torque and thrust measured at different tip speed ratios (TSRs) and the other turbine parameters, such as self-starting velocity, working characteristic curve, as well as the yaw-angle effect. Together with CFD simulation results, design optimization can be carried out, particularly through adjusting blade installation angles, various pitch angles, and so on. After this, sea test on site can be carried on in order to complete the final test of the turbine.

The DUTTCT is a horizontal TCT which is designed and made by the Dalian University of Technology (DUT) research group. Numerical and experimental investigations have been conducted for examining the turbine hydrodynamic performance. Here, the methods and results of the investigations are detailed in this paper.

In the rest of the paper, experiments including experiment design, test implementation, and test results are reported in the Experimental Tests section. Numerical investigations including methodology and simulation results are presented in the Numerical Simulations and Investigations section, which is followed by discussions and conclusions in the Conclusions and Discussions section.

Experimental Tests

The horizontal tidal current turbine, called DUTTCT, is designed and built at DUT [18]. The TCT is designed for use in the Bohai Sea and the Huanghai Sea in China, where there is low tidal current velocity ranging from 1 m/s to 2 m/s. At the current

stage, the turbine is only designed for the purpose of theoretical and experimental studies. The sketch of the DUTTCT impeller is shown in Fig. 1, and its detailed parameters are shown in Table 1.

Experimental equipment including the turbine, yaw, and support as well as measurement and control systems are designed to carry out hydrodynamic performance tests in a towing tank for the DUTTCT. The overall design sketch is shown in Figs. 2 and 3 shows a picture of the experimental setup.

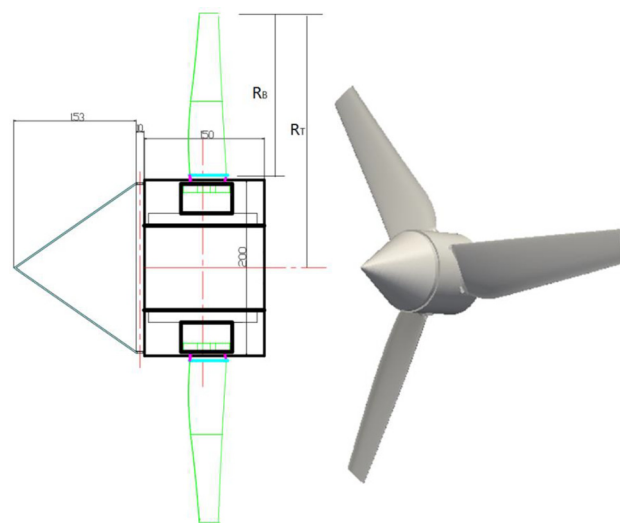


Fig. 1 The sketch of DUTTCT impeller

Table 1 The blade parameters of DUTTCT

Item	Parameters
Radius of impeller	$R_T = 0.57 \text{ m}$
Length of blade	$R_B = 0.47 \text{ m}$
Number of blades	$Z_T = 3$
Swept area	$S_T = 1.02 \text{ m}^2$

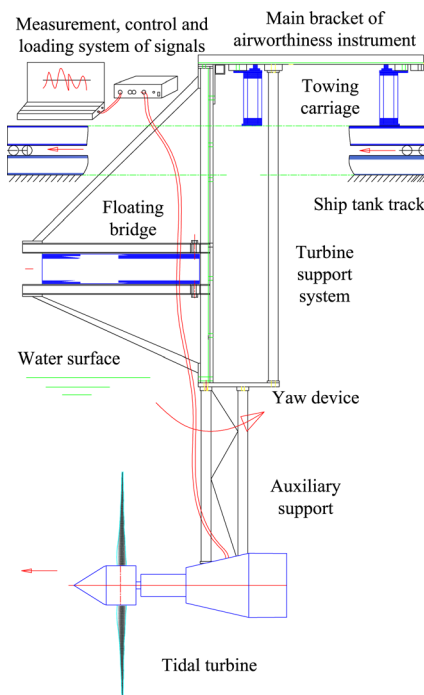


Fig. 2 Overall design sketch of DUTTCT experiment



Fig. 3 A picture of the DUTTCT experimental equipment

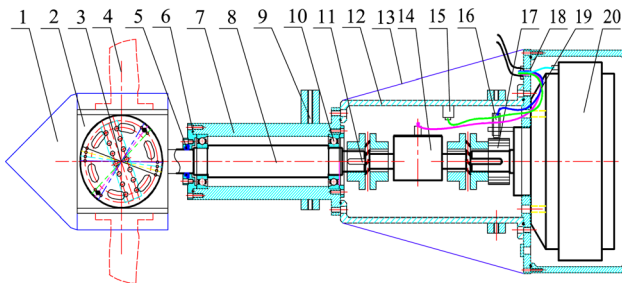


Fig. 4 A sketch of the experimental setup

Design of DUTTCT Experimental System. The DUTTCT experimental setup consists of a turbine, transmission and braking systems, and sealing which are shown in Fig. 4. The components include the following: (1) front dome, (2) hub, (3) pitch device, (4) blades, (5) motive seal, (6) static seal of joint faces, (7) bearing box, (8) main shaft, (9) auxiliary support, (10) deep groove ball bearing, (11) diaphragm coupling, (12) sensor box, (13) rear dome, (14) torque sensor, (15) acceleration sensor, (16) rotational speed sensor, (17) rotational speed gear, (18) cable hose static seal, (19) cable, and (20) magnetic powder brake.

Turbine Design. A hydrofoil is designed using a weight superposition method which combines two cardinal foils: NACA 6 series and S805. The specified hydrofoil is utilized for the DUTTCT blade which is made of aluminum alloy 5083. A rectangular blade root is adopted and installed on a flange by bolt. Then, the flange is fixed on a triangular hub, forming a three-bladed turbine rotor. The rotor is connected to the main shaft through inner holes of the hub. The parameters of the turbine are shown in Table 2.

Design of Transmission and Sealing Systems. The two ends of the main shaft are constrained by deep groove ball bearings. The main shaft is connected to a magnetic powder brake by a torque sensor. In order to offset misalignment, soft diaphragm couplings are used on the two ends of the torque sensor. The sealing system includes a motive seal for the rotating main shaft and static seals for joint faces and cable hose. The TVM200350-T46 single-acting sealing element from Trelleborg Company is adopted for motive seal, while static seals are made of rubber rings.

Table 2 Structure parameters of DUTTCT turbine

Category	Unit	Value
Blade chord	m	0.05–0.16
Blade length	m	0.5
Preset pitch angle	deg	-9 to +9
Blades number	—	3
Turbine diameter	m	1.1
Shaft diameter	m	0.05
Rotation speed	rpm	80–300

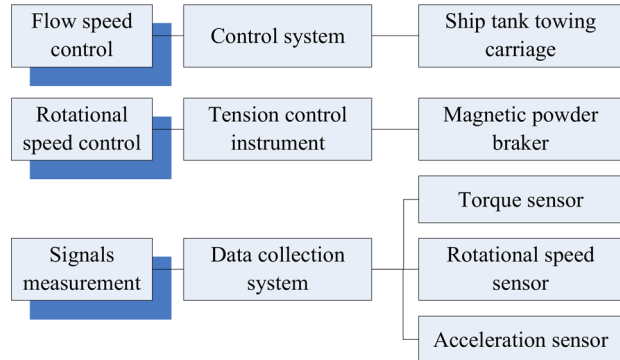


Fig. 5 The schematic diagram of the systems for measurement, control, and loading system

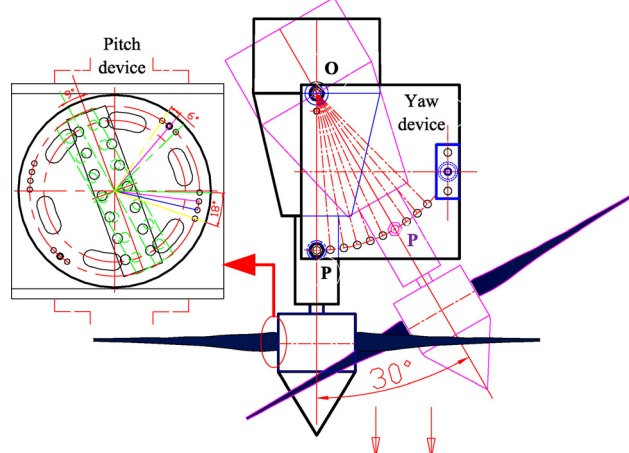


Fig. 6 The schematic diagram of the yaw and pitch device

Design of Measurement, Control, and Loading Systems. Signals such as rotational speed, flow speed, torque, and vibration are to be measured. The schematic diagram of the systems for collecting those signals mentioned previously is shown in Fig. 5.

Water flow speed is controlled by a towing trailer with an accuracy of ± 0.05 m/s, and the speed is assumed to be steady.

Design of Yaw System. The direction and magnitude of tidal current flow in the real world would change periodically. Therefore, a yaw device is designed so that the hydrodynamic performance of the DUTTCT due to yaw effect could be observed. A schematic diagram of the yaw device is shown in Fig. 6.

A yaw plate is used to enable the turbine to turn over some specified angles. It rotates around a pivot point O anticlockwise with radius OP. The interval is 5 deg and the maximum 45 deg. The bolt at point O and P are fixed after rotation is over.



Fig. 7 The supporting structure of the DUTTCT

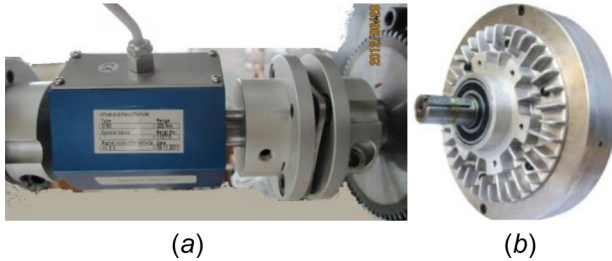


Fig. 8 Torque sensor (a) and magnetic powder brake (b)

Design of the Supporting System. The towing trailer includes the main supporter of airworthiness instrument, floating bridge, etc. According to the practical structure of boat pool trailer, the supporting system of the DUTTCT experimental equipment is designed by a combination of triangular brackets and truss structures as shown in Fig. 7.

Measuring Instruments

Torque sensor. A commercial torque sensor called Messtechnik 0180 is adopted, whose measurement range is 200 N·m and its accuracy is 1% (The Messtechnik 0180 is produced by Lorenz Messtechnik GmbH, Alfdorf, Germany). The sensor is sealed in a chamber for underwater use. Its outside diameter and length are smaller than 120 mm and 160 mm, as shown in Fig. 8(a).

Magnetic powder brake. A magnetic powder brake, based on electromagnetic principle, uses magnetic powder to transmit torque. The magnetic powder brake is capable of starting, buffering, braking, loading, and power absorption. In the experiment, the PB-10 type magnetic powder brake is selected with 100 N·m rated torque, 1–2 N·m starting torque, 1800 rpm allowable rotation speed, direct current 24 V supply voltage, and 3 A maximum current as shown in Fig. 8(b).

Monitoring and controlling systems. A digital display table is used to promptly display rotation speed and torque while dynamic signals are recorded by dynamic data acquisition instrument, and these data are processed and analyzed by an industrial personal computer. Rotation speed, torque, and vibration of the turbine are monitored by sensors and the signals are recorded by dynamic data acquisition instrument. The dynamic load exerting on the brake could be controlled by the digital display table system. The monitoring and controlling systems are shown in Fig. 9.

Boat pool trailer. The turbine experimental equipment is installed on a trailer, which could move at different speeds for emulating tidal current flow conditions. The tank is 160 m long, 8 m wide, and 3.7 m deep, and the trailer speed range is 0.05–8.0 m/s (see Fig. 10). An all-digital SIEMENS control system with ± 0.05 m/s speed accuracy is adopted.

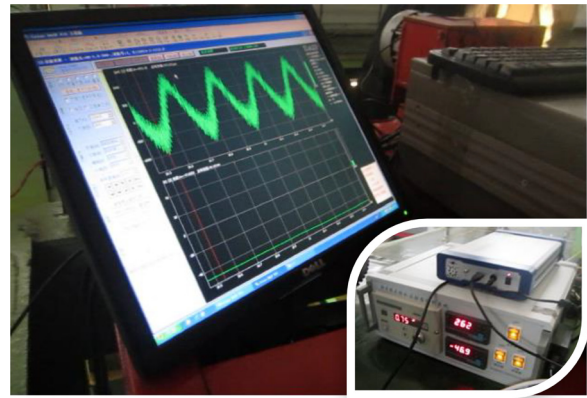


Fig. 9 A photo of the control and monitoring systems



Fig. 10 A photo of the DUT towing tank

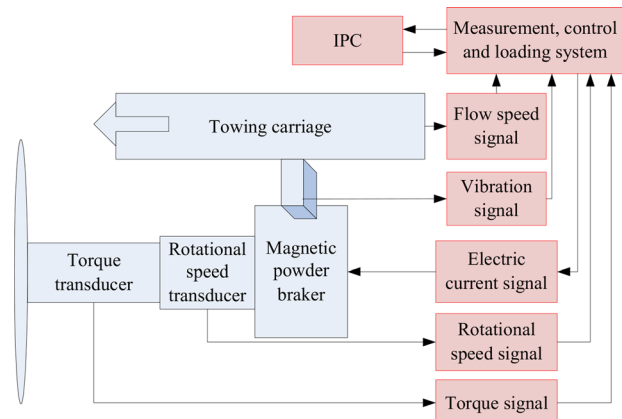


Fig. 11 A schematic diagram of the experimental system

The functions and operational principles of the experimental equipment are shown in Fig. 11 as a summary of this section.

Experimental Setup. Experiments for studying the hydrodynamic performance of the DUTTCT are described in Table 3.

Turbine Self-Starting Tests. In the self-starting tests, the magnetic powder brake is kept closed before the experiment. The trailer starts with the acceleration of 0.1 m/s^2 and holds its speed after it reaches predetermined flow speed. Time history diagrams

Table 3 Conditions of experiments

Category	Flow speed (m/s)	Rotational speed (rpm)	Magnetic powder brake
Self-starting test	0.8 0.75 0.745 0.725	Automatic (four times)	Off
Tests for TSR and yaw effects	0.8	89.6–120.4 (five times)	Adjusting to stabilize rotational speed
20 deg yaw test	1.75 0.8 1.75	110.6–228.0 (ten times) 90–108.86 (three times) 118.3–216.0 (three times)	

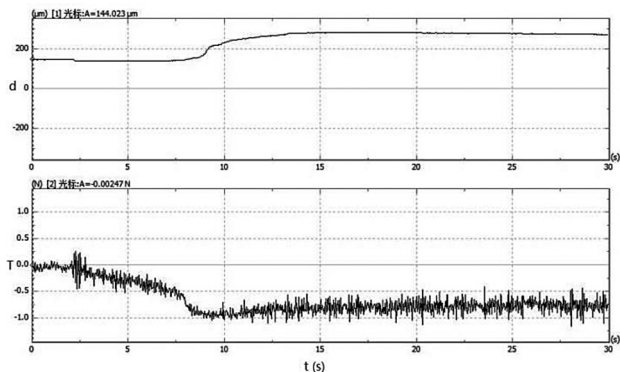


Fig. 12 Time history of gear displacement (above) and torque (down) at 0.725 m/s

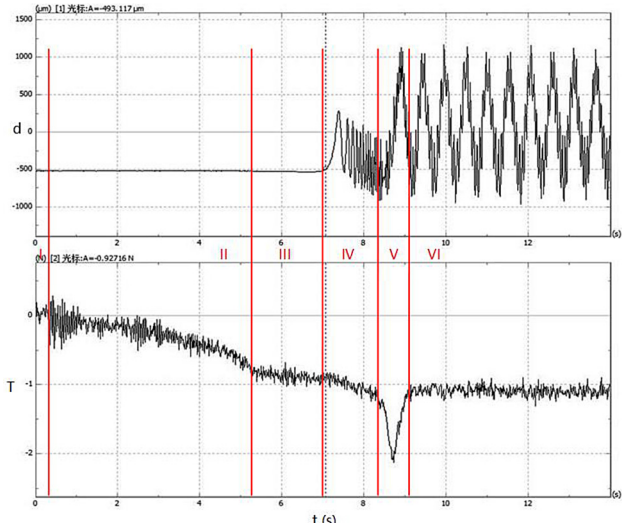


Fig. 14 Time history of gear displacement (above) and torque (down) at 0.75 m/s

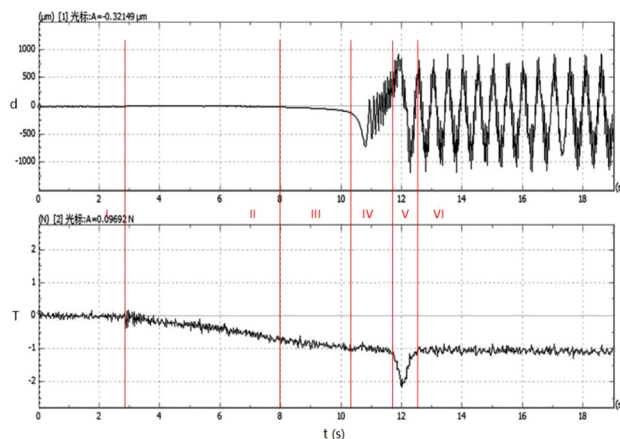


Fig. 13 Time history of gear displacement (above) and torque (down) at 0.745 m/s

of gear (70 teeth) displacement (its frequency is rotational speed) and torque are, respectively, recorded and plotted in Figs. 12–14 for flow speeds 0.725 m/s, 0.745 m/s, and 0.75 m/s, respectively.

There are six phases found in those time historical data in Figs. 12–14, which are indicated by vertical lines. Considering Fig. 14 as an example, phase I denotes standstill of the trailer. In phase II, the torque starts to jitter and rapidly increases with oscillation (negative). In phase III, the torque is basically steady, and in phase IV, the displacement jitter of the rotational speed of the gear occurs with high frequency and torque slightly increases. In phase V, the turbine starts and at this time, the torque increases sharply and promptly decreases to the original value before the start. There is maximum torque in this phase. In phase VI, the rotational speed enters a steady running stage. The torque is kept constant at about $-1\text{ N}\cdot\text{m}$.

Table 4 Comparison of starting times and starting torques

Flow speed (m/s)	Time of every phase (s)					Maximum torque (N·m)
	II	III	IV	V	Sum	
0.800						-2.245
0.750	4.9	1.7	1.4	0.8	8.8	-2.132
0.745	5.2	2.3	1.4	0.9	9.8	-2.159
0.725						-0.950

A comparison of starting times for different self-starting cases is summarized in Table 4.

It is shown that the self-starting velocity for the DUTTCT system is about 0.745 m/s, and maximum torque is about $2.159\text{ N}\cdot\text{m}$. In fact, the self-starting velocity is meant for the whole system, not just for the turbine alone. There are two components for torque: One is the part to overcome friction force generated by the motive seal, while the other is to overcome the shaft torque from loadings. In our lab, we measure the torque required by motive seal by wrench torque before loadings are installed and find that its value is $2\text{ N}\cdot\text{m}$. In the case of incoming flow velocity at 0.725 m/s, torque increases to near $-1\text{ N}\cdot\text{m}$ at first, and then reduces slightly and remains constant about $-0.75\text{ N}\cdot\text{m}$. The turbine could not start to rotate without enough torque.

Effects of Tip Speed Ratio and Yaw on Turbine Performance. According to the experiments planned, in each TSR and yaw experiment, a predetermined flow speed is prescribed, and the torque of magnetic powder brake is then adjusted in order to

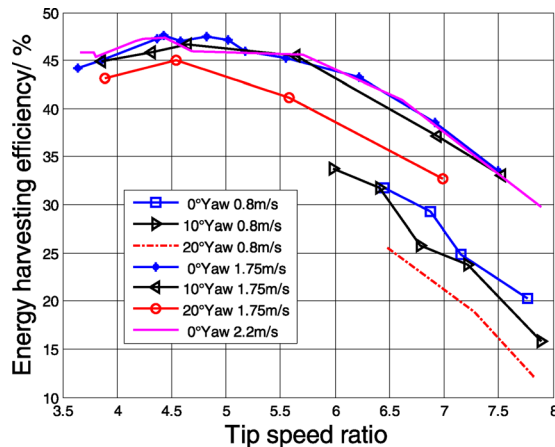


Fig. 15 Efficiencies versus TSR for the DUTTCT

obtain the required turbine rotating speed, thus the predetermined TSR. The signals of rotational speeds and torques during the whole process are recorded. The time-averaged torque and rotating speed are used in experimental data analysis. The characteristic curves of energy conversion efficiency versus tip speed ratio are shown in Fig. 15.

The results show that energy conversion efficiency increases as TSR increases from 3.5 to 4.5 and then decreases as TSR further increases from 4.5 to 7.5. The optimum tip speed ratio is about 5 for the proposed turbine, and the corresponding efficiency is 47.6% in the experiment. The lowest tip speed ratio is limited to 3.64 since the corresponding rotation speed, 110.6 rpm, is beyond the measurement range of the system.

Yaw effects are also investigated in this section. There are two sets of data for yaw effects obtained by experiments corresponding to incoming velocities at 0.8 m/s and 1.75 m/s, respectively. The yaw angle for each incoming flow is set to 0 deg (no yaw angle), 10 deg, and 20 deg, respectively. Figure 15 shows that energy conversion efficiency with 10 deg yaw decreases slightly, by less than 1%, compared with the corresponding result of the zero yaw case for an incoming velocity at 0.8 m/s. As for the case of incoming velocity at 1.75 m/s, the efficiency value does not decrease too much, by only about 2–3%, compared with the value of zero yaw angle. There is a maximum value at about 45% with $TSR = 4.5$ for all cases. When the yaw angle increases to 20 deg, the situations for the two incoming velocities are very different, and their efficiency difference is large by comparison with the results of lower yaw angles. For example, for the case of incoming velocity at 0.8 m/s, the profile of efficiency at 20 deg yaw angle is almost parallel to that of zero yaw angle, and the efficiency of the former is lower than the latter by about 5–6%. With incoming velocity at 1.75 m/s and a yaw angle of 20 deg, different from the smooth characteristic curves for zero yaw angle or 10 deg yaw angle as TSR varies from 3.5 to 6, and a sharp profile of efficiency is obtained for the same TSR range. These indicate that larger yaw angles will have greater negative impacts on the conversion of energy, which should be avoided during operations.

Numerical Simulations and Investigations

Numerical simulations and investigations are conducted after the experiment for the purpose of mutual validation with experimental data and supplementing incomplete experimental data, as well as for the in-depth analysis of flow patterns. For example, there is a lack of data for working characteristic curves as TSR is less than 3.64 in the experiment due to the mismatch of magnetic powder brake.

As discussed previously, the MRF method is traditionally used in CFD studies to investigate flow fields in rotating machinery. However, the DOD for three-bladed tidal current/stream turbines

is normally low. Thus, it is more accurate to use the ALE method with a rotating mesh around the rotating rotor and an AMI to connect it to a stationary mesh in the DUTTCT.

In this paper, the PIMPLEDYMFOAM, which is an ALE solver based on the hybrid pressure-implicit with splitting operators-semi-implicit method for pressure linked equation (PIMPLE) numerical solution algorithm and dynamic meshes (DYM) with the AMI from the open-source software openFOAM4.x [12] and its predecessor called TURBODYMFOAM, is used to perform the numerical simulations. In the Mathematical Formulae for PIMPLEDYMFOAM section, the details of the governing equations for fluid flows used in the software and numerical simulations are presented.

Mathematical Formulae for PIMPLEDYMFOAM. The governing equations for unsteady incompressible flows used by PIMPLEDYMFOAM are the Navier–Stokes equations as described in following equations in vector form:

$$\frac{\partial \mathbf{W}}{\partial t} + \nabla \cdot \mathbf{F}_C = \nabla \cdot \mathbf{F}_V \quad (1)$$

$$\mathbf{W} = \begin{bmatrix} p \\ u \\ v \\ w \end{bmatrix} \quad \mathbf{F}_c = \begin{bmatrix} \mathbf{U} \\ (u - u_m)\mathbf{U} + p\delta_{ij} \\ (v - v_m)\mathbf{U} + p\delta_{ij} \\ (w - w_m)\mathbf{U} + p\delta_{ij} \end{bmatrix} \quad \mathbf{F}_v = \begin{bmatrix} 0 \\ \frac{1}{Re} \cdot \nabla \cdot u \\ \frac{1}{Re} \cdot \nabla \cdot v \\ \frac{1}{Re} \cdot \nabla \cdot w \end{bmatrix} \quad (2)$$

where \mathbf{W} is the flow parameter vector, \mathbf{U} is the velocity vector, u_m is the grid velocity vector, p is pressure, ρ is density, and Re is the Reynolds number. The finite volume method is used to discrete the previously mentioned governing equations, and the details of its numerical discretization could be found in the references given in Refs. [19–23].

As mentioned in the Introduction section, the application of PIMPLEDYMFOAM to the numerical simulation of TCTs has not yet been reported in the literature. For the sake of accuracy and reliability, PIMPLEDYMFOAM was first validated by using the data of an European Research Community on Flow, Turbulence, and Combustion centrifugal pump, including comparisons with experimental data and numerical results by ANSYS CFX [18]. After this, PIMPLEDYMFOAM is then used to numerically study the performance of the DUTTCT and results obtained are analyzed and compared with the data obtained by experiment described in the Experimental Tests section.

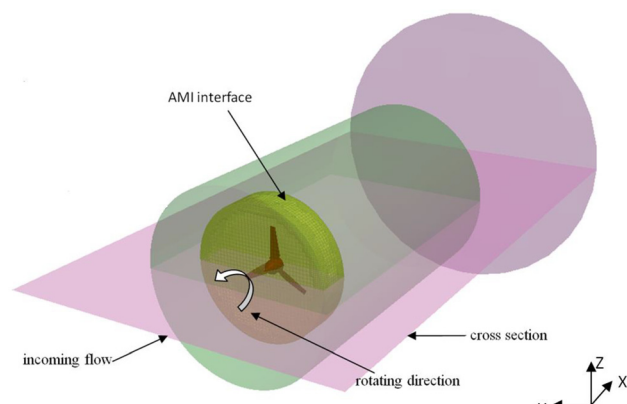


Fig. 16 The sketch of AMI for DUTTCT in the computational domain. (The largest cylinder denotes the computational domain; the smallest cylinder surface represents the AMI; and the smallest cylinder indicates the refinement domain around the turbine and wake region.)

Table 5 The sizes of computational domain

Item	Sizes
Diameter of outer cylinder	$D_O = 5 \text{ m}$
Height of outer cylinder	$H_o = 8.5 \text{ m}$
Diameter of inner cylinder	$D_i = 3.2 \text{ m}$
Height of inner cylinder	$H_i = 4.6 \text{ m}$
Diameter of AMI cylinder	$D_{AMI} = 2 \text{ m}$
Height of AMI cylinder	$H_{AMI} = 0.5327 \text{ m}$

Table 6 Initial conditions and some parameters for the computational cases

Item	Parameters
Current speed	$U_T = (0.5-2) \text{ m} \cdot \text{s}^{-1}$
Viscosity coefficient	$\frac{\mu_T}{\mu} = 10$
Turbulent kinetic energy k	$k = \frac{3U_0^2 I^2}{2}$
Turbulent dissipation rate	$\varepsilon = \frac{C_\mu \rho k^2}{\mu_T} = \frac{C_\mu \rho k^2}{\mu(\mu_T/\mu)}$
Outlet pressure	$p = 0$
Rotation angular velocity	$\omega = 0, (600-1000) \text{ deg} \cdot \text{s}^{-1}$
Kinematic viscosity	$\nu = 10^{-5} \text{ m}^2 \cdot \text{s}^{-1}$
Media density	$\rho = 1000 \text{ kg} \cdot \text{m}^{-3}$

Table 7 Boundary conditions of the computational model

Item	Filename	Parameters
Inlet speed	0/U	$(0.5-2) \text{ m} \cdot \text{s}^{-1}$
Outlet pressure	0/p	$p = 0$
The type of AMI boundary	All files in directory 0	cyclic AMI
Rotation angular velocity	Constant	$0, (600 \sim 1000) \text{ deg} \cdot \text{s}^{-1}$

Table 8 Constant parameters for standard $k-\varepsilon$ model in PIMPLEDYMFOAM

Name	Value
C_μ	0.09
$C_{\varepsilon 1}$	1.44
$C_{\varepsilon 2}$	1.92
C_ε	1.3

Table 9 Self-starting simulation cases

Case number	Current speed ($\text{m} \cdot \text{s}^{-1}$) (c)	Acceleration ($\text{m} \cdot \text{s}^{-2}$) (a)
Case-1-c-a ^a	0.5, 0.55, 0.6, 0.65, 0.7, 0.75, 0.8	0, 0.1, 0.5

^aThe affiliated definitions of case-1-c-a: “1” denotes a self-starting simulation case, “c” represents the current speed, and “a” indicates the acceleration. For example, case-1-0.5-0.1 means the self-starting simulation case with a current speed of 0.5 m/s and an acceleration of 0.1 m/s². With those current speeds and accelerations shown in Table 6, there are totally 21 cases for self-starting simulations.

Computational Domain of the DUTTCT. Figure 16 shows the rotation direction of the blades and the AMI boundary in the computational domain. Pink cylinder denotes the whole computational domain, the surface of yellow-green cylinder the AMI boundary, and the red part the impeller. The dimensions of the computational domain are shown in Table 5.

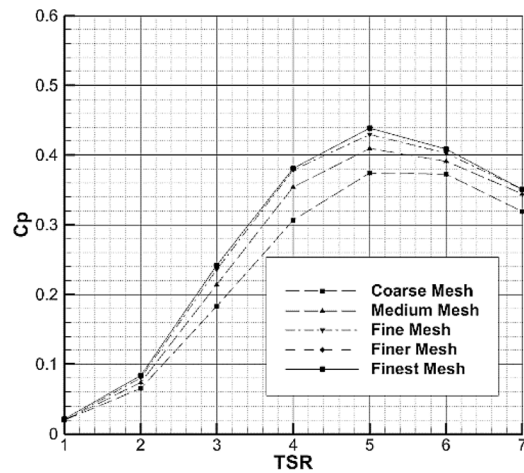
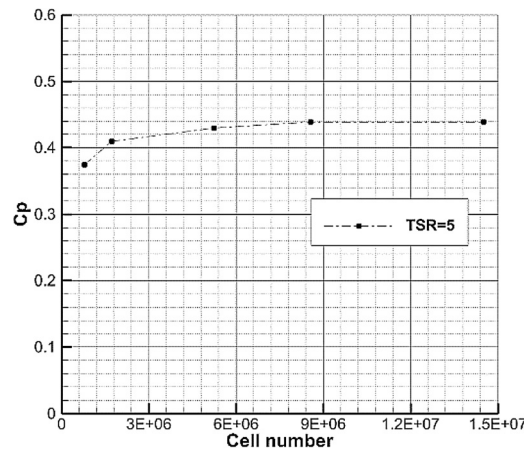
Table 10 Simulation cases for working characteristic curves

Case number	Current speed ($\text{m} \cdot \text{s}^{-1}$) (c)	TSR (t)
Case-2-c-t ^a 1-255	1, 1.25, 1.5, 1.75, 2.0	2, 2.5, 3, 3.5, 4, 4.5, 5, 5.5, 6, 6.5, 7

^aThe affiliated definitions of case-2-c-t: “2” denotes working a characteristic simulation case, c represents the current speed, and “t” denotes the TSR. For example, case-2-1.25-2.5 means the working characteristic simulation case with a current speed of 1.25 m/s and a TSR of 2.5. With those current speeds and TSRs shown in Table 7, there are totally 55 cases for working characteristic simulations.

Table 11 Mesh information in mesh convergence tests

Cases	Stationary domain	Rotating domain	Whole domain
Coarse mesh	260,000	530,000	790,000
Medium mesh	530,000	1,200,000	1,730,000
Fine mesh	940,000	4,300,000	5,240,000
Finer mesh	1,360,000	7,200,000	8,560,000
Finest mesh	1,360,000	13,150,000	14,510,000

**Fig. 17** Mesh convergence results with a speed of 1 m/s**Fig. 18** Mesh convergence results with TSR = 5

Model Setup. Table 6 lists the initial conditions and some parameters used for the simulation cases, while Table 7 specifies the boundary conditions, and in Table 8, the parameters for the standard $k-\varepsilon$ model are given.

The Simulation Cases. There are two sets of simulations conducted in the numerical investigation of the DUTTCT: (1) self-starting cases; (2) simulations performed to obtain its characteristic curves. The detailed information of these cases is described in Tables 9 and 10. In the self-starting cases, the rotational angular velocity of the turbine is initially set to zero, and the incoming flow speeds are varied from 0.5 m/s to 0.8 m/s with a speed interval 0.05 m/s. Besides, three accelerations, 0, 0.1, and 0.5 m/s², are used to simulate the accelerating options of the tow truck in the towing tank. In the second set, both incoming flow velocity and rotational angular velocity are fixed in each simulation, and the TSR is varied from 2 to 7.

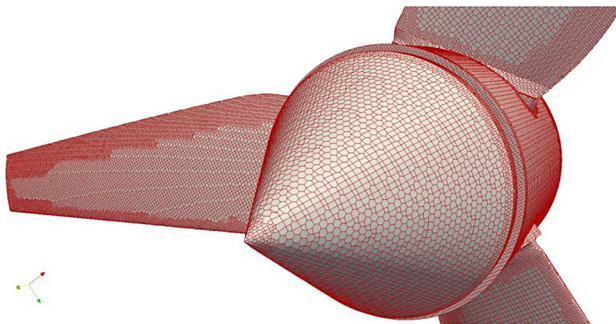


Fig. 19 Surface mesh on the DUTTCT generated by SnappyHexMesh

Mesh Convergence Tests. Before all the full numerical simulations for the DUTTCT, mesh convergence tests are conducted first. There are five mesh grids used in the mesh convergence test, which are generated by using a mesh generation tool, SnappyHexMesh, provided by openFOAM. During the mesh generation, the mesh inside the green cylinder (as shown in Fig. 16) in the stationary domain is refined, while the grid outside the green cylinder in the stationary domain is kept the same. There is one exception where the meshes are the same for both finer and finest meshes in the stationary domain. The mesh details are summarized in Table 11. There are a total of seven TSRs chosen in the mesh convergence tests.

Figure 17 shows the results of mesh convergence tests in the form of turbine performance characteristic curves with seven TSRs and an incoming velocity of 1 m/s. The simulation results indicate that it is necessary to test mesh convergence through different TSRs. The simulation solutions become convergent as the fine mesh used. Figure 18 shows the mesh convergence results for the case of TSR = 5, which demonstrate that the power efficiency is gradually convergent with increasing mesh density. Due to the limitation of computer resources and computing time available, the fine grid is finally chosen to perform numerical investigations in the following simulation cases. The $y+$ value around blade surfaces for the fine mesh varies from 26 to 280, and the average value is about 173, which is valid for the implementation of the k-epsilon turbulence model. Figure 19 shows the surface mesh generated by SnappyHexMesh.

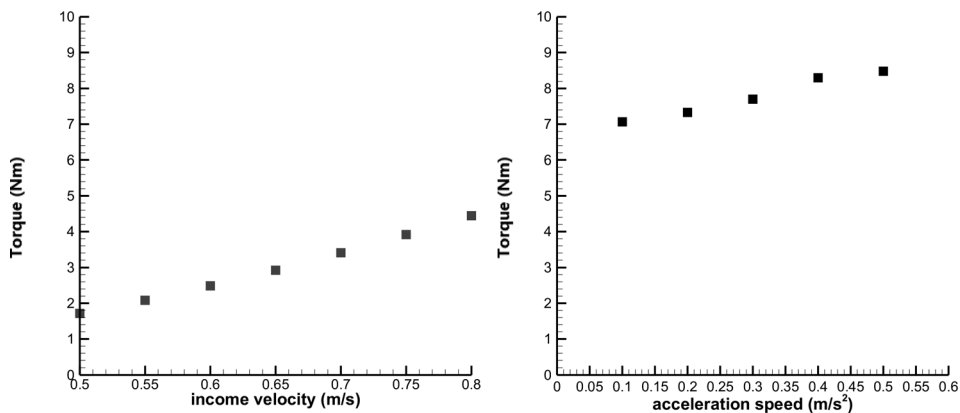


Fig. 20 Calculated maximum torques versus different incoming velocities (left) and accelerations to 1 m/s (right)

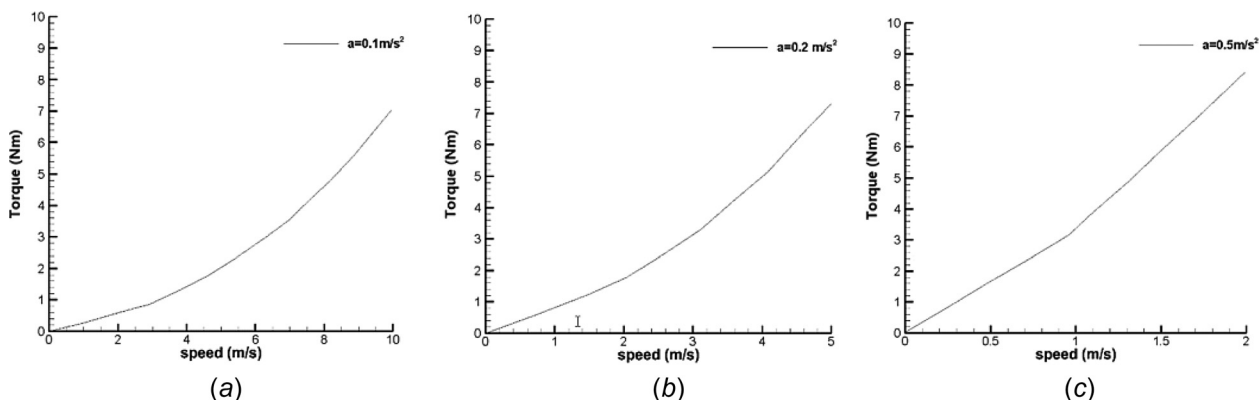


Fig. 21 Calculated torques versus incoming velocities during constant accelerations: (a) $a = 0.1 \text{ m/s}^2$, (b) $a = 0.2 \text{ m/s}^2$, and (c) $a = 0.5 \text{ m/s}^2$

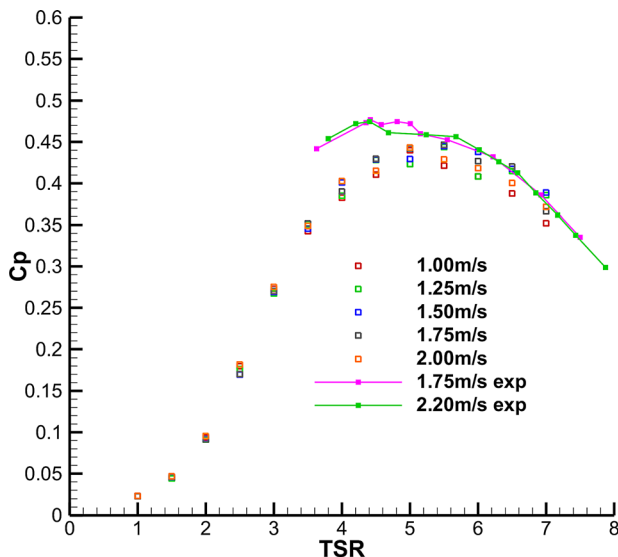


Fig. 22 The working characteristic curves of the DUTTCT

Numerical Results

Self-Starting Performance of the DUTTCT. In order to understand the self-starting behavior of the DUTTCT, two types of incoming velocities have been studied in this section, which are constant incoming velocity and variable incoming velocity,

respectively. The former represents the idealized steady-state conditions, while the later shows the real accelerating processes of the towing truck as in the experiment in the towing tank. Based on the experimental results, the self-starting velocity for the DUTTCT is about 0.75 m/s, which could be seen in Table 4 in the Experimental Tests section. Hence, the constant incoming velocities in the tests are chosen to be between 0.5 m/s and 0.8 m/s, and the turbine is stationary in the beginning. Figure 20 shows the calculated torques exerting on the turbine shaft with different incoming velocities. The torque of the DUTTCT is increasing from about 1.75 N·m at 0.5 m/s to approximately 4.6 N·m at 0.8 m/s linearly. In fact, the torque required for self-starting measured by the torque wrench is about 2.0 N·m, which means that the DUTTCT would start to rotate when the incoming velocity is greater than 0.55 m/s. Figure 20 also plots torques versus incoming velocity as it is increased from 0 to 1 m/s with different accelerations. In fact, the acceleration considered in the paper is larger than the tidal flow accelerations in real engineering applications. The purpose of considering the acceleration effect is to compare the numerical results with the experimental ones. The towing tank in the experiment has three accelerations, 0.1 m/s^2 , 0.2 m/s^2 , and 0.5 m/s^2 , respectively. Figure 20 shows that the torque increases faster and reaches higher values with the increase of acceleration. As incoming velocity reaches 1 m/s, the value of torque for the case of 0.5 m/s^2 is 8.6 N·m, 1.5 N·m larger than that for the case of 0.1 m/s^2 . Acceleration has a significant influence on the self-starting behavior of a turbine. Normally, one only concerns about the self-starting of a turbine with constant incoming velocity, which is hardly found in actual applications, because tidal flow velocity usually varies both in time and space. Therefore, the issue of acceleration should be

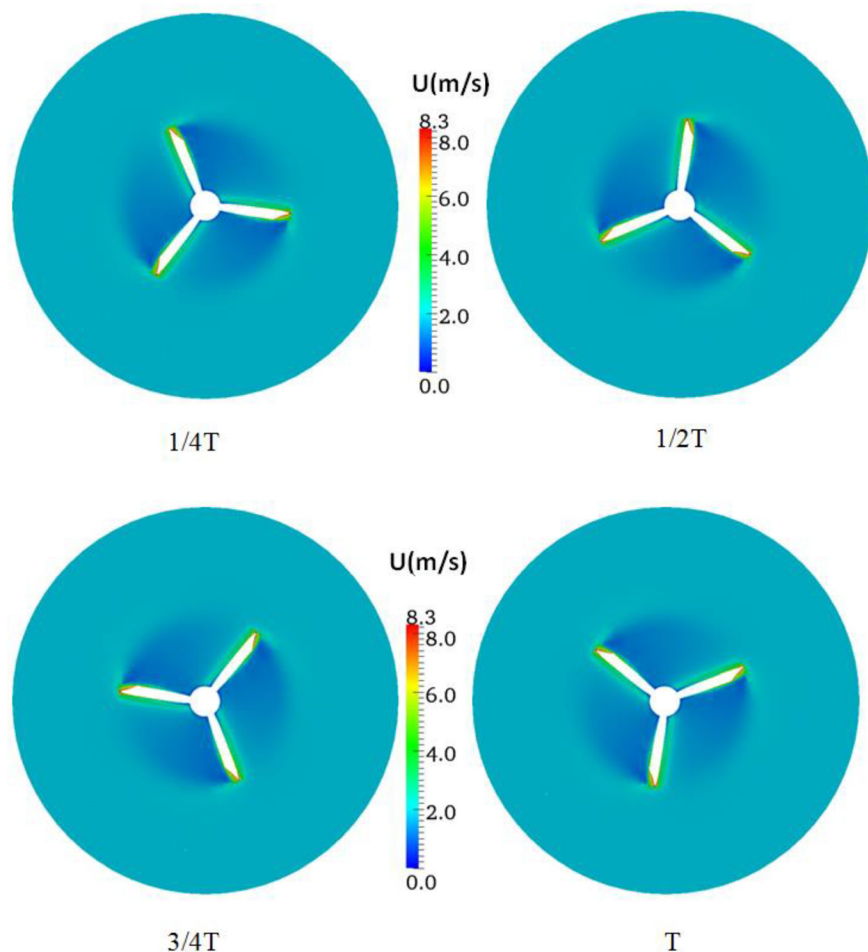


Fig. 23 Velocity contours at different instants in case-2-1.75-5.5

highly relevant when self-starting is assessed for a tidal current turbine.

Figure 21 presents the torque results of case-1-0.5-0.1, case-1-0.5-0.2, and case-1-0.5-0.5. When incoming velocity increases during accelerations, the torque increases in a quadratic manner, which is different from the results of constant incoming velocity. Furthermore with larger accelerations, higher torques are obtained as can be seen clearly in Fig. 21.

The Characteristic Curves of the DUTTCT. The working characteristic curves show three most important factors of the turbine: the highest efficiency of the turbine, the optimal TSR, and the high-efficiency range of TSR. After the completion of all simulation cases, the characteristic curves of the DUTTCT are summarized in Fig. 22. It shows that the highest efficiency is about 45% at an optimal TSR of 5.5, and for TSR ranging from 3.5 to 7, the efficiency of the DUTTCT is above 40%. The output efficiency does not show significant variations with various incoming velocities in which the value of Reynolds number changes from 1.81×10^6 to 5.08×10^6 . For the purpose of comparison, those experimental data given in the towing tank experiment are also plotted in Fig. 22. A good agreement between the simulation and experimental results is obtained for larger TSRs from TSR = 5. However, the efficiencies obtained from the experiment shown in Fig. 22 are slightly larger than the numerical results in the range from TSR = 3–5. There are two possible reasons for the discrepancies: One may be due to the turbulence model used in the CFD simulations with lower TSR and thus lower Reynolds number values, while the other may be due to experimental errors in the torque and rotating speed measurements. Nevertheless, based on the curves obtained in Fig. 22, the DUTTCT has indeed good working performance with various low incoming velocities in a wide range of TSRs.

Wake Flow Analysis. Wake flow behind the turbine is important for the design of turbine farms. The turbine should be designed to be installed and positioned in the farm with little/or no influence of the wake flow produced by other turbines. In this section, a numerical investigation on wake flow produced by the DUTTCT for a specific case (incoming velocity at 1.75 m/s, and TSR at 5.5) is carried out. In order to better illustrate wake patterns, pressure contours and velocity distributions have been plotted at several time instants in one period.

Figure 23 shows velocity contours at four different instants: $1/4T$, $1/2T$, $3/4T$, and T at $x=0$, here x is the rotating axis and T denotes the time for the turbine to rotate one cycle, and $T = (2\pi)/\omega$, where ω is the angular velocity of the turbine.

Figure 23 shows that there is a large area in the cross section with a velocity of about 1.75 m/s, which indicates that the majority of the coming fluid flows through the impeller section directly, and only the fluid around the blade area is affected. This is due to a low DOD we mentioned at the beginning of this section. Furthermore, velocity around the blades has a special nonuniform distribution. The maximum speed is 8.3 m/s at the blade's tip as the rotational angular velocity is 834 deg/s (139 rpm). Generally, the flow velocity decreases when fluid passes through the blades. According to energy conservation, the flow kinetic energy is transformed into pressure energy which is, in turn, taken up by the blades to generate the torque and power output. This results in the flow velocity reduction and low pressure in the wake region.

In order to study the flow patterns in the wake region, five lines are chosen in the plane of xz . Figure 24 shows the sketches of these five lines and their relative positions to the impeller for $1/4T$, $1/2T$, $3/4T$, and T time instants from both side view and front view.

Pressure and velocity distributions along with the five lines are shown in Fig. 25. Although there are no blades sweeping through xz plane at $1/4T$ moment, it is clear that both pressure and velocity experience the historical effect produced by the three rotating blades. The same phenomena could be found at other three time

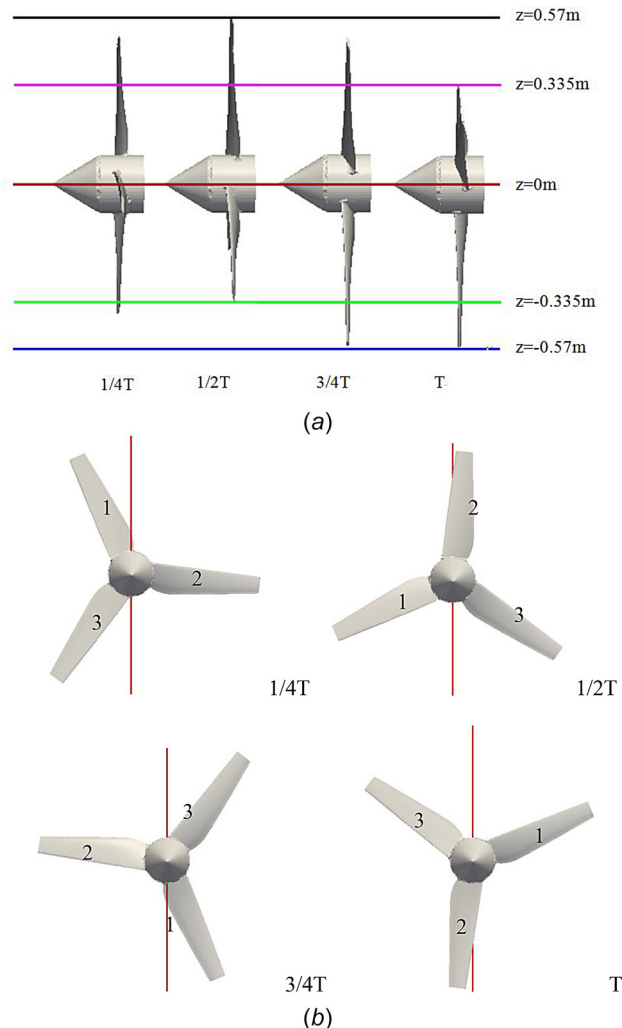


Fig. 24 Five lines chosen at different z positions: (a) side view and (b) front view. (The central plane of the rotor is located at $x = 2.31$ m.)

instants, which prove that the flow passing through the blades is unsteady. The steady assumption used in the theory of BEM may result in errors, which has also been addressed in a number of publications concerning BEM, for example, Ref. [8]. Moreover, comparing with the values along $z = 0.57$ m and $z = -0.57$ m, both pressure and velocity distributions are different, especially those values around the rotating plane. The differences become even larger when the wake flow pattern along $z = 0.335$ m and $z = -0.335$ m is taken into consideration. It is clear that the distributions of both pressure and velocity in the circular direction are not uniform. Again, the uniform assumption in circular direction used in BEM may result in errors. Hence, it can be concluded that the actual flow around a tidal turbine is much more complicated than the assumptions made in the theory of BEM, and the flow is really 3D and turbulent. Only through CFD simulation, hydrodynamic performances of tidal stream/current turbines can be fully analyzed.

At $1/2T$, the tip of blade one is approaching the line $z = 0.57$ m, and the speed increases rapidly. Incident stream has a sharp pressure increase with a difference of normalized pressure of about $3.7 \text{ m}^2/\text{s}^2$. The difference in pressure along the line $z = 0.335$ m is about $2.2 \text{ m}^2/\text{s}^2$. The variation in pressure produces torque to drive the blades. Along the line $z = 0$ m, the distributions of pressure and velocity are the same at the four time instants. The pressure difference is caused by the obstruction of the hub to the flow. At $3/4T$ and T instants, the distributions of pressure and velocity

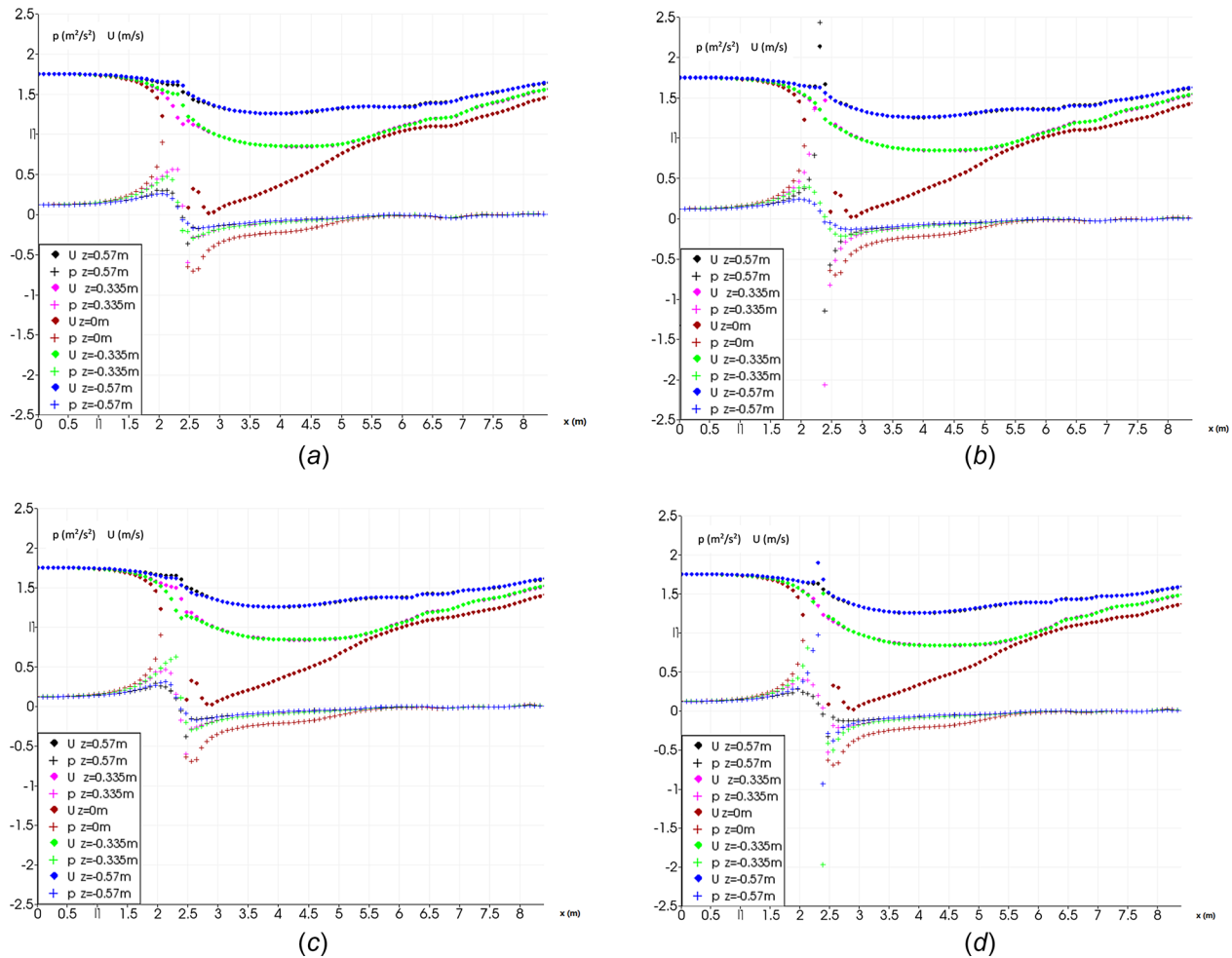


Fig. 25 Pressure and velocity distributions along five lines at four different time instants: (a) $1/4T$, (b) $1/2T$, (c) $3/4T$, and (d) T . (The central plane of the rotor is located at $x = 2.31 \text{ m}$.)

along the five lines are symmetrical about the z -axis with those at $1/4T$ and $1/2T$ instants, respectively.

Pressures on Blade Surfaces. Figure 26 shows the pressure distributions on both suction and pressure surfaces of the DUTTCT blades. The suction surface of the blade has negative pressure regions while the pressure on pressure surface of the blade is always positive. Particularly, there are cone-shaped areas of negative pressure formed on the pressure surfaces, which extend to the tips and will reduce the torque and then the output efficiency. In order to further investigate the effect of negative pressure on pressure surfaces, pressure contours around the DUTTCT blades are shown in Fig. 27 with modified ranges of pressure legends. As we can see in Fig. 27, the conical-shaped negative pressure on pressure surfaces near the blade tips will result in resistance to rotor

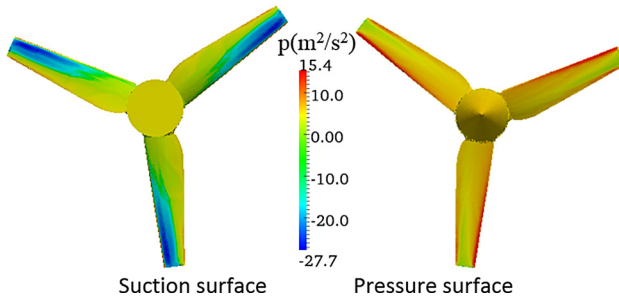


Fig. 26 Pressure contours on blade surfaces of the TCT

rotation in the anticlockwise direction. This means that the blade design can be improved in order to get rid of the negative pressure areas on the pressure surfaces, which may be due to fluid flowing from the positive pressure surfaces around the tips onto the

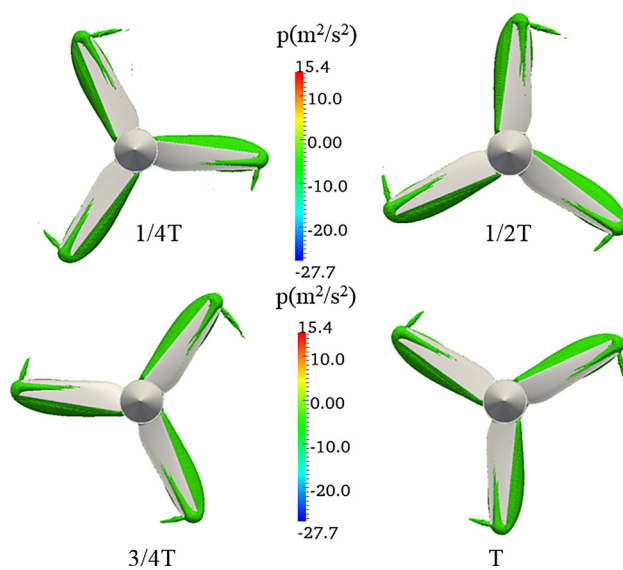


Fig. 27 Pressure contours around the DUTTCT blades at different time instants

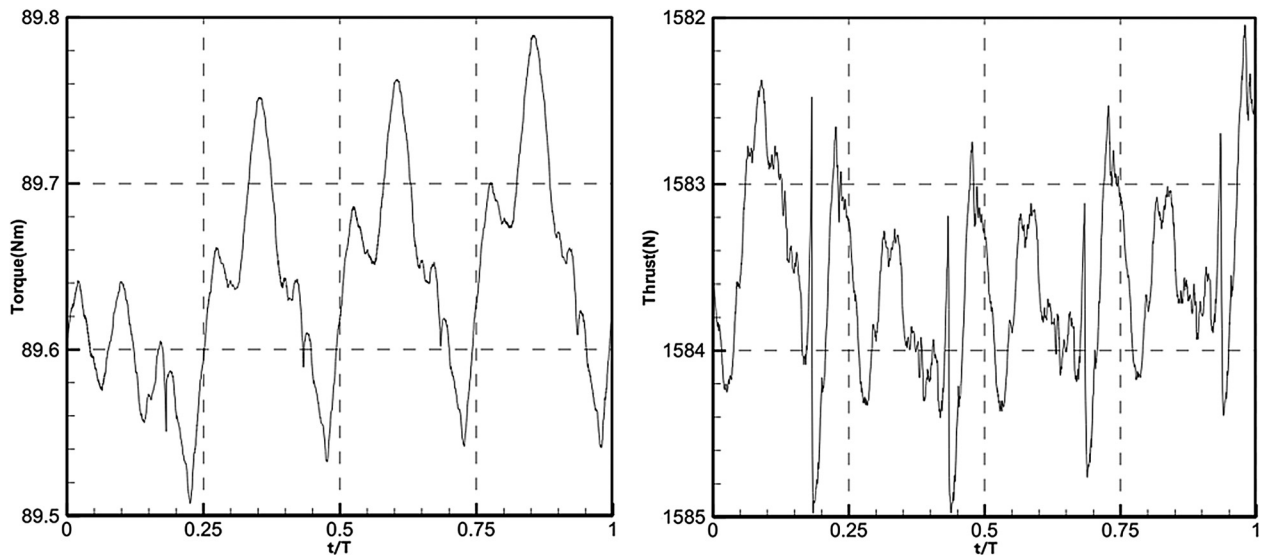


Fig. 28 The profiles of torque and thrust in one period for case-2-1.75-5.5

negative ones. Furthermore, another negative area is found on the tail of the blade tip, which is due to blade tip vortices, again as a result of the pressure differences near the blade tips.

The time histories of the torque and thrust in one period are plotted in Fig. 28. The range of torque is from 89.5 N·m to 89.8 N·m for case-2-1.75-5.5, while the range of thrust is from 1582 N to 1585 N. The averaged torque is 89.63 N·m in one period while the averaged thrust is 1583.5 N. The results indicate that the loading on blades is quite stable when the turbine is working at constant incoming velocity and rotating speeds. The thrusts obtained are positive in the positive x direction, which is the incoming velocity direction as shown in Fig. 28.

Conclusions and Discussions

In this paper, the hydrodynamic performance of the DUTTCT has been investigated experimentally and numerically. The findings obtained in the numerical and experimental investigations are very valuable for further improvement of the turbine performance and also provide valuable experience for future research work on tidal current turbines. The major conclusions about the DUTTCT are as follows:

- (1) The results show that the maximum power conversion efficiency of the DUTTCT could reach up to 47.6%, and all the power efficiencies are over 40% for TSRs ranging from 3.5 to 6. Its self-starting velocity is about 0.745 m/s, while the self-starting torque is about 2 N·m. The yaw angle does not affect its efficiency significantly when it is less than 10 deg. The DUTTCT has good working performance with low freestream velocities in a wide range of TSRs.
- (2) The flow patterns and pressure distributions in the wake region are found to be much more complicated than the steady and two-dimensional assumptions made in the theory of BEM, and the flow is indeed 3D and turbulent. CFD technology can be used to check and validate the design of tidal turbines originally designed by the BEM theory. This can also be employed for further design optimization.
- (3) Numerical simulations and experimental tests should be conducted simultaneously to complement and validate each other. For example, the power characteristic curves obtained from experiments lack lower range TSR values because of the mismatched magnetic powder brake. However, numerical simulation results provide valuable low range TSR data.

Funding Data

- The Natural Science Foundation of Liaoning Province, China (Project No. 2015020629).

References

- [1] Uihlein, A., and Magagna, D., 2016, "Wave and Tidal Current Energy—A Review of the Current State of Research Beyond Technology," *Renewable Sustainable Energy Rev.*, **58**, pp. 1070–1081.
- [2] Liu, H. W., Ma, S., Li, W., Gu, H. G., Lin, Y. G., and Sun, X. J., 2011, "A Review on the Development of Tidal Current Energy in China," *Renewable Sustainable Energy Rev.*, **15**(2), pp. 1141–1146.
- [3] Li, D., Wang, S. J., and Yuan, P., 2010, "An Overview of Development of Tidal Current in China: Energy Resource, Conversion Technology and Opportunities," *Renewable Sustainable Energy Rev.*, **14**(9), pp. 2896–2905.
- [4] Li, W., Zhou, H. B., Liu, H. W., Lin, Y. G., and Xu, Q. K., 2016, "Review on the Blade Design Technologies of Tidal Current Turbine," *Renewable Sustainable Energy Rev.*, **63**, pp. 414–422.
- [5] Li, Y., 2014, "On the Definition of the Power Coefficient of Tidal Current Turbines and Efficiency of Tidal Current Turbine Farms," *Renewable Energy*, **68**, pp. 868–875.
- [6] Zhao, Y., and Su, X. H., 2010, "Tidal Energy: Technologies and Recent Developments," *IEEE International Energy Conference and Exhibition*, Manama, Bahrain, Dec. 18–22, pp. 618–623.
- [7] Zhou, Z. B., Benbouzid, M., Charpentier, J. F., Scuiller, F., and Tang, T. H., 2017, "Developments in Large Marine Current Turbine Technologies—A Review," *Renewable Sustainable Energy Rev.*, **71**, pp. 852–858.
- [8] Churchfield, M., Li, Y., and Moriarty, P., 2013, "A Large-Eddy Simulation Study of Wake Propagation and Power Production in an Array of Tidal-Current Turbines," *Philos. Trans. R. Soc. A*, **371**(1985), p. 20120421.
- [9] Wang, S. Q., Sun, K., Xu, G., Liu, Y. T., and Bai, X., 2017, "Hydrodynamic Analysis of Horizontal-Axis Tidal Current Turbine With Rolling and Surging Coupled Motions," *Renewable Energy*, **102**(Part A), pp. 87–97.
- [10] Elie, B., Oger, G., Guillerm, P.-E., and Alessandrini, B., 2017, "Simulation of Horizontal Axis Tidal Turbine Wakes Using a Weakly-Compressible Cartesian Hydrodynamic Solver With Local Mesh Refinement," *Renewable Energy*, **108**, pp. 336–354.
- [11] Bai, G. H., Li, W., Chang, H., and Li, G. J., 2016, "The Effect of Tidal Current Directions on the Optimal Design and Hydrodynamic Performance of a Three-Turbine System," *Renewable Energy*, **94**, pp. 48–54.
- [12] OpenFOAM, 2014, "OpenFOAM Programmer's Guide 2.3.0," The OpenFOAM Foundation Ltd., London.
- [13] Lawson, M. J., Li, Y., and Danny, C. S., 2011, "Develop and Verification of a Computational Fluid Dynamics Model of a Horizontal-Axis Tidal Current Turbine," *ASME Paper No. OMAE2011-49863*.
- [14] Jing, F. M., Ma, W. J., Zhang, L., Wang, S. Q., and Wang, X. H., 2017, "Experimental Study of Hydrodynamic Performance of Full-Scale Horizontal Axis Tidal Current Turbine," *J. Hydraul.*, **29**(1), pp. 109–117.
- [15] Gaurier, B., Davies, P., Deuff, A., and Germain, G., 2013, "Flume Tank Characterization of Marine Current Turbine Blade Behaviour Under Current and Wave Loading," *Renewable Energy*, **59**, pp. 1–12.
- [16] Bahaj, A. S., Molland, A. F., Chaplin, J. R., and Batten, W. M. J., 2007, "Power and Thrust Measurements of Marine Current Turbines Under Various

- Hydrodynamic Flow Conditions in a Cavitation Tunnel and a Towing Tank," *Renewable Energy*, **32**(3), pp. 407–426.
- [17] Bahaj, A. S., Batten, W. M. J., and McCann, G., 2007, "Experimental Verifications of Numerical Predictions for the Hydrodynamic Performance of Horizontal Axis Marine Current Turbines," *Renewable Energy*, **32**(15), pp. 2479–2490.
- [18] Zhang, K. L., 2013, "Numerical Study of Horizontal Tidal Current Turbine by Using PimpleDyMFoam," *Master's thesis*, Dalian University of Technology, Dalian, China.
- [19] Holzmann, T., *Mathematics, Numerics, Derivations and OpenFOAM(R)*, Holzmann CFD, Leoben, Austria.
- [20] Jasak, H., 1996, "Error Analysis and Estimation for the Finite Volume Method With Applications to Fluid Flows," *Ph.D. thesis*, Imperial College London, London.
- [21] Jasak, H., and Gosman, A. D., 2003, "Element Residual Error Estimate for the Finite Volume Method," *Comput. Fluids*, **32**(2), pp. 223–248.
- [22] Jasak, H., Weller, H. G., and Gosman, A. D., 1999, "High Resolution NVD Differencing Scheme for Arbitrarily Unstructured Meshes," *Int. J. Numer. Methods Fluids*, **31**(2), pp. 431–449.
- [23] Weller, H. G., Tabor, G., Jasak, H., and Fureby, C., 1998, "A Tensorial Approach to Computational Continuum Mechanics Using Object-Oriented Techniques," *Comput. Phys.*, **12**(6), pp. 620–631.